Journal of Manufacturing Science and Engineering. Received June 04, 2019;
Accepted manuscript posted October 28, 2019. doi:10.1115/1.4045418

Effects of varying dynamics of flexible workpieces in milling operations

Adam K. Kiss
Department of Applied Mechanics
Budapest University of
Technology and Economics,
MTA-BME Lendület Machine Tool
Vibration Research Group,
Budapest, Hungary
Email: kiss_a@mm.bme.hu

Daniel Bachrathy
Department of Applied Mechanics
Budapest University of
Technology and Economics,
MTA-BME Lendület Machine Tool
Vibration Research Group,
Budapest, Hungary
Email: bachrathy@mm.bme.hu

Gabor Stepan
Department of Applied Mechanics
Budapest University of
Technology and Economics
Budapest, Hungary
Email: stepan@mm.bme.hu

In this study, surface error calculations and stability conditions are presented for milling operations in case of slender parts. The dynamic behavior of the flexible beam-type workpiece is modeled by means of Finite Element Method (FEM), while the varying dynamical properties related to the feed motion as well as the material removal process are incorporated in the model. The FEM-generated direct Frequency Response Function is verified through a closed form solution based on the distributed transfer function method. Relative errors and convergence of the FEM are investigated based on the analytical solutions of the continuum model, from which, appropriate element size and mode number can be selected for modal coordinate transformations. The pattern in the variation of the natural frequencies is explored using the analytical model in case of high radial depth of cut relative to the original cross-section of the beam-like workpiece. Both the stability conditions and the resulted surface errors are predicted as a function of the tool position. The presented approach and the results are validated by laboratory tests.

1 Introduction

Cutting is a widely used manufacturing method, however, this kind of machining process can be disturbed by harmful vibrations that can reduce the life of the machine tool and the surface quality. It is an important task to provide the reliable prediction of machine tool vibrations, both in terms of increasing productivity and minimizing costs and losses. The most accepted explanation for the large amplitude machine tool vibrations (chatter) is the so-called surface regenerative effect [1], where the position of the previous cutting edge influences the chip cross-section [2], which can be described by delayed differential equations [3].

The range of chatter-free technological parameters is usually represented in so-called stability charts, which are determined by the stability of the stationary solution of the corresponding mathematical model. In the last decades, several numerical methods have been developed to calculate these stability charts in order to support the technological design. Without completeness, we mention:

i) the methods in time domain such as the semi-discretization method [4], the full-discretization method [5], the integration method [6], the Chebyshev collocation method [7] and the temporal finite element analysis [8];

ii) the methods in frequency domain such as the zero-order approximation (ZOA) [9], the multi-frequency solution (MFS) [10] or the extended multi-frequency solution (EMFS) [11].

In time domain, the dynamical behavior of the model can be described by means of the identification of the modal parameters, which is a complex engineering procedure itself. An advantage of the frequency domain solutions is that they can directly use the measured Frequency Response Function (FRF) after applying some filtering technique.

For high precision machining, for example, the errors of the machined surface are still relevant even in case of stable machining operations. These surface errors may appear dur-

ing both turning and milling processes. In case of stable turning, there is an offset error generated by the constant cutting force [12]. Due to the intermittent characteristics of milling processes, relative vibrations are induced between the tool and the workpiece even in case of stable cutting operations. Consequently, not just the so-called Surface Location Error (*SLE*) appears, but also the surface roughness (*R*) [13,14,15]. In [16], the surface location errors and the stability lobe diagram are presented together on a so-called superchart.

It is well known that the dynamical characteristics of the CNC machine and the workpiece significantly influence the behavior of the machining process. It is an essential task to predict this dynamical behavior precisely in order to construct a reliable superchart, from which, one can select robust parameter combinations to reach high material removal rate [17]. The dynamical properties may vary during machining due to the different configurations of the machine tool structure within the workspace [18, 19, 20, 21] and due to the variation of the workpiece geometry according to the material removal [17, 22, 23, 24]. The latter is dominant for thin-walled structures, so it is essential to take these changes into account. Finite Element Method (FEM) is a natural choice for modelling thin-walled workpieces and to trace the dynamical properties during material removal [25, 26, 27].

Although finite element method can be used for any complex workpiece geometry, the model and the associated FE mesh have to be updated frequently to make it follow the variation of the geometry due to the material removal process. This requires significant computational time and effort [25]. The modal matrices of the FEM are quite large for an appropriately densed finite element mesh. Thus, it requires significant computational effort to obtain the stationary solutions of the milling process and to determine their stability. One way to decrease the size of the matrices and to save computational cost is the application of modal coordinate transformation [28] by considering only a few dominant vibration modes [29].

The sufficient number of modes and the resolution of the FE mesh have to be selected appropriately to reach proper balance between accuracy and computational needs. These parameters are usually determined based on test cases for which analytical solution exists.

In this study, we analyze the dynamical behavior of a flexible workpiece model that can be used in both for turning and for milling processes. For this reason, we use a beam-type workpiece, which is complex enough to capture all aspects of the varying workpiece dynamics, but simple enough for analytical modeling. Note that for complex models such as turbine blade, pocket milling, rib machining, cutting tubular and thin walled parts the change in the dynamic properties are very problem specific and it is difficult to draw a general conclusion.

First, the model based on FEM is generated for Bernoulli beam elements, which is later compared to the exact FRF of the workpiece. Using a suitable Green function, the closed analytical form is based on the distributed transfer function method (DTFM) [30]. This eliminates the need for finite element discretization and the need for solving the large eigenvalue-eigenvector problem, which may require high computational resources [31]. Then we examine the FE mesh resolution and the number of considered modes in the modal transformation to obtain the parameters of sufficiently accurate FRF for stability and surface error calculations.

Usually, in case of a general industrial machining process, the technological parameters are already given, such as tool path relating to workpiece geometry, cutting tool and other machining parameters, they are technology-dependent. Modifications only in the spindle speed and the feed rate are allowed due to these limitations from the industrial side.

With this model, we examine in details how dynamic properties change as a function of the tool position according to the material removal process of cutting. In the next step, stability chart and surface property calculations are developed using an FRF based model for milling operation. The variations of the dynamic properties caused by the material removal and the changing tool position are also considered. Finally, the predicted phenomena are identified by measurement results.

The paper is organized as follows: in Section 2, we provide the FRF based on FEM model of the workpiece which is validated through analytical FRF. Then, in Section 3, the effects of the feed motion are analyzed with respect to the dynamical parameters. In this section, an extreme case is illustrated, from which, one can get a picture into the changing dynamics of the underlying system. Section 4 gives the governing equation of milling process together with the corresponding stability and surface error calculations. A case study is conducted in Section 5 with numerical and measurement results, where we analyze the machined surface quality and investigate the effects of the feed motion. Finally, in Section 6, we summarize conclusions and discuss future research directions.

2 Dynamics of the workpiece

In this section, we describe the mechanical model of the cutting process, with special attention on the dynamic behavior of the flexible workpiece while the material removal process is also taken into account.

During the machining process, the cutting tool's actual position along its path determines the location of the contact region, that is, the resulting cutting force acts only at the actual contact point identified by the coordinate e in Fig. 1. In the dynamical models, only the relative vibrations between the tool and the workpiece are included. Therefore, only the direct FRF, with excitation and response at the same position, have to be taken into account in the stability and surface error calculations.

From the dynamical point of view, the workpiece dynamics can change significantly during the cutting process in two different ways [32]. One corresponds to the varying contact position, which is taken into account by means of the variation of the modal stiffness through the corresponding mode shapes. The other one relates to the effects of the material removal process. According to the feed motion, the

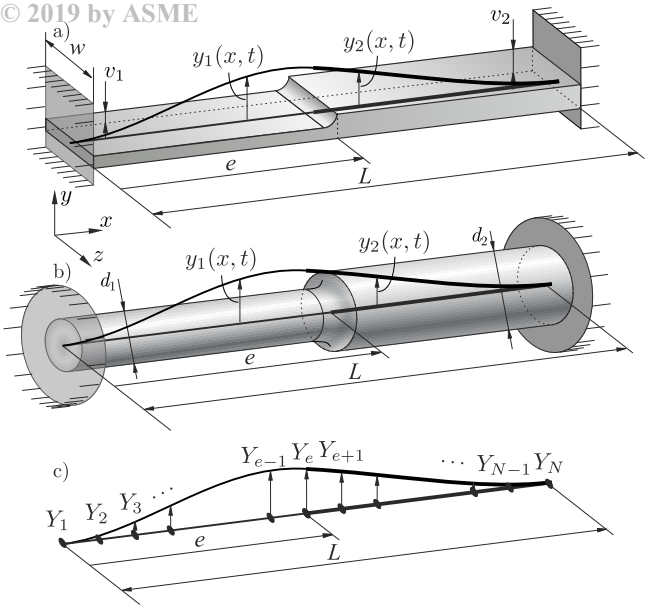

Fig. 1. Schematic figure of the applied beam-type workpiece considering the material removal for milling (a) and turning (b) processes.

cross section is reduced along the preceding tool path. This leads to changing workpiece geometry and correspondingly varying dynamical parameters, especially in the natural frequencies of the workpiece.

Due to the reason that one of the main scope of this contribution is to explore the behavior of the varying dynamics, the workpiece is assumed to be much more flexible compared to the cutting tool together with the whole machine tool structure. This assumption is valid for thin walled workpieces [19], as shown for example in Fig. 1. Thus, the cutting tool and the workpiece are assumed to be rigid and a flexible, respectively. Note that for a given workpiece geometry, the appropriate modal matrices can be extracted from most of the industrial FEM software. In addition, one can include the dynamic characteristic of the cutting tool and the machine tool and can extend the model by means of measuring and adding the tool tip FRF to the computed workpiece FRF [18,21,33].

2.1 Discrete model of the workpiece

The mechanical model of the flexible workpiece during the machining process is shown in Fig. 1c. It is assumed that the transverse dimensions are negligible relative to the longitudinal one. In this case, the horizontal (longitudinal) vibration is not modeled, since the structure is more rigid in this direction compared to the transverse one. According to these assumptions, bending vibration dominates the model, which justifies the consideration of a beam model. For the actual tool position e, the governing equation assumes the form

$$\mathbf{M}(e)\ddot{\mathbf{Y}}(t)+\mathbf{C}(e)\dot{\mathbf{Y}}(t)+\mathbf{K}(e)\mathbf{Y}(t)=\mathbf{v}(e)F_y(t), \quad (1)$$

where the deformation of the workpiece is described by the N-dimensional generalized coordinate vector $\mathbf{Y}$ and the dynamical parameters are defined by means of the mass, damping and stiffness matrices as $\mathbf{M}(e)$, $\mathbf{C}(e)$ and $\mathbf{K}(e)$, respectively. On the right hand side, the general force vector is composed as a product. Its first term is the vector $\mathbf{v}(e)$ that represents the actual contact position; all its elements are zero expect the unitary one of the element at the $\mathrm{int}(1+(N-1)e/L)^{\mathrm{th}}$ coordinate. The second term, $F_y(t)$ describes the cutting-force component in the y direction, which is time periodic in case of milling process. Following the assumption in [34, 35], the dynamics of the feed motion is considered to be slow relative to the fast dynamics of $\mathbf{Y}(t)$ and $F(t)$, that is, the variation of the tool position e is considered to be quasi-static [36].

Up to this point, Eq. (1) can describe both milling and turning processes. The only difference between them is the cutting force in the right-hand side, which is discussed in details in Sec. 4.

According to the theory of modal analysis [29], in case of proportional damping, the equation of motion in Eq. (1) can be given as decoupled equations of each modal coordinate ξ_k. After transforming to the frequency domain of ω, it reads as

$$\begin{aligned}-\omega^2\xi_k(\omega)+\mathrm{i}\omega 2\zeta_k(e)\omega_{\mathrm{n},k}(e)\xi_k(\omega)+\omega_{\mathrm{n},k}^2(e)\xi_k(\omega)\\ =\phi_k(\omega),\end{aligned} \quad (2)$$

where $\phi_k(\omega)$ is the modal force of the k^{th} mode shape, $\omega_{\mathrm{n},k}(e)$ is the k^{th} undamped natural angular frequency and $\zeta_k(e)$ is the modal damping of the k^{th} mode shape, ($k=1,2,...,m$, where m is the number of the modes). In case of proportional damping, the damping coefficients $\zeta_k(e)$ can be calculated as

$$\zeta_k(e)=\frac{\alpha_{\mathrm{M}}}{2\omega_{\mathrm{n},k}(e)}+\frac{\alpha_{\mathrm{K}}}{2}\omega_{\mathrm{n},k}(e), \quad (3)$$

where α_{M} and α_{K} are the proportional damping coefficients in $\mathbf{C}=\alpha_{\mathrm{M}}\mathbf{M}+\alpha_{\mathrm{K}}\mathbf{K}$ (see [29]). With a FEM based model, the slow variation of the FRF can be given for each mode. The corresponding scalar valued direct FRF $H(\omega,e)$ is given as a function of the frequency ω and the tool position e:

$$\tilde{H}(\omega,e)=\sum_{k=1}^{\tilde{m}}\frac{\tilde{T}_{\mathrm{e},k}^2(e)}{-\omega^2+\mathrm{i}\omega 2\tilde{\zeta}_k(e)\tilde{\omega}_{\mathrm{n},k}(e)+\tilde{\omega}_{\mathrm{n},k}^2(e)}, \quad (4)$$

where $\tilde{T}_{\mathrm{e},k}(e)$ is the element of the k^{th} mass normalized mode shape vector at the contact point and $\tilde{m}\leq m$ is the number of relevant modes. Tilde denotes the approximation of the exact FRF. The discrete model tends to the exact FRF only if the element size of the corresponding FE mesh tends to zero and the number of considered modes tends to infinity.

2.2 Distributed parameter model

In order to validate the FEM model, we present the mathematical background of the closed-form expression of

FRF through the derivation of the bending vibration of continuum beams based on DTFM [30]. Since there is a sharp change in the geometry of the cross section at the tool position e, the total length L of the workpiece is distingushed with index i along the x coordinate of beam. In the displacement function $y_i(x,t)$, the subscript i refers to the corresponding section: $i=1$ for the part that has already been machined ($x\in[0,e]$), while $i=2$ for the intact part ($x\in[e,L]$). The linearized equations of motion form the partial differential equations [37,38,39]

$$\begin{aligned}&\rho A_i\ddot{y}_i(x,t)+c_{\mathrm{M}i}\dot{y}_i(x,t)+c_{\mathrm{K}i}\dot{y}_i''''(x,t)+I_{\mathrm{z}i}Ey_i''''(x,t)=\\&\frac{1}{2}F_y(x,t)\delta(x-e),\quad i=1,2;\end{aligned}\tag{5}$$

with the corresponding boundary conditions

$$\begin{aligned}y_1(0,t)=0,\quad y_1'(0,t)=0,\\y_2(L,t)=0,\quad y_2'(L,t)=0\end{aligned}\tag{6}$$

at the clamped ends, and the interface conditions

$$\begin{aligned}&y_1(e,t)=y_2(e,t),\qquad y_1'(e,t)=y_2'(e,t),\\&I_{\mathrm{z}1}y_1''(e,t)=I_{\mathrm{z}2}y_2''(e,t),\ I_{\mathrm{z}1}y_1'''(e,t)=I_{\mathrm{z}2}y_2'''(e,t)\end{aligned}\tag{7}$$

that describe the smooth connection between the two segments. Prime stands for differentiation with respect to the spatial coordinate x. The material parameters ρ and E are the density and the young modulus, respectively. Also, $c_{\mathrm{M}i}$ and $c_{\mathrm{K}i}$ are the proportional damping coefficients, which are related to the proportional damping coefficients (see in Eq. (3)): $c_{\mathrm{M}i}=\alpha_{\mathrm{M}}\rho A_i$ and $c_{\mathrm{K}i}=\alpha_{\mathrm{K}}I_{\mathrm{z}i}E$.

The cross sections are characterized with area A_i and area moment of inertia (or second moment of area) $I_{\mathrm{z}i}$. Note that the governing equation Eq. (5) is suitable to model the beam-like workpiece during milling and turning processes (see Fig. 1ab), but the parameters A_i and $I_{\mathrm{z}i}$ are calculated with different formulas.

Laplace transform of Eq. (5) leads to

$$\begin{aligned}&\left(s^2\rho A_i+sc_{\mathrm{M}i}\right)\overline{y}_i(x,s)+\left(sc_{\mathrm{K}i}+I_{\mathrm{z}i}E\right)\overline{y}_i''''(x,s)=\\&\frac{1}{2}\overline{F}_y(x,s)\delta(x-e),\ i=1,2;\end{aligned}\tag{8}$$

where $\overline{y}(x,s)=\mathcal{L}(y(x,t))$ and $\overline{F}_y(x,s)=\mathcal{L}(F_y(x,t))$ are the Laplace transforms of $y(x,t)$ and $F_y(x,t)$, respectively, and $s\in\mathbb{C}$ represents the complex Laplace domain.

We introduce the following state space vector

$$\boldsymbol{\eta}_i(x,s)=\left(\overline{y}_i(x,s)\ \overline{y}_i'(x,s)\ \overline{y}_i''(x,s)\ \overline{y}_i'''(x,s)\right)^{\mathrm{T}}\tag{9}$$

and the corresponding excitation vector

$$\boldsymbol{\Phi}_i(x,s)=\left(0\ 0\ 0\ \frac{\overline{F}_y(x,s)\delta(x-e)}{2(sc_{\mathrm{K}i}+I_{\mathrm{z}i}E)}\right)^{\mathrm{T}}.\tag{10}$$

Therefore, the governing equation and the corresponding boundary conditions in Eqs. (5) and (6)-(7) can be written as a first-order ordinary differential equation

$$\boldsymbol{\eta}'(x,s)=\mathbf{A}(s)\boldsymbol{\eta}(x,s)+\boldsymbol{\Phi}(x,s),\tag{11}$$

with boundary conditions

$$\mathbf{P}\boldsymbol{\eta}(0,s)+\mathbf{Q}\boldsymbol{\eta}(e,s)+\mathbf{R}\boldsymbol{\eta}(L,s)=\mathbf{0},\tag{12}$$

where $\boldsymbol{\eta}(x,s)=(\boldsymbol{\eta}_1(x,s)^{\mathrm{T}}\ \boldsymbol{\eta}_2(x,s)^{\mathrm{T}})^{\mathrm{T}}$ and $\boldsymbol{\Phi}(x,s)=(\boldsymbol{\Phi}_1(x,s)^{\mathrm{T}}\ \boldsymbol{\Phi}_2(x,s)^{\mathrm{T}})^{\mathrm{T}}$. The coefficient matrix of Eq. (11) can be given as

$$\mathbf{A}(s)=\begin{pmatrix}\mathbf{A}_1(s) & \mathbf{0}\\ \mathbf{0} & \mathbf{A}_2(s)\end{pmatrix},\tag{13}$$

where

$$\mathbf{A}_i(s)=\begin{pmatrix}0 & 1\,0\,0\\ 0 & 0\,1\,0\\ 0 & 0\,0\,1\\ -\frac{s^2\rho A_i+sc_{\mathrm{M}i}}{sc_{\mathrm{K}i}+I_{\mathrm{z}i}E} & 0\,0\,0\end{pmatrix},\tag{14}$$

and $\mathbf{0}$ stands for the 4×4 zero matrix. The coefficient matrices

$$\mathbf{P}=\begin{pmatrix}\mathbf{I}\,\mathbf{0}\,\mathbf{0}\,\mathbf{0}\\ \mathbf{0}\,\mathbf{0}\,\mathbf{0}\,\mathbf{0}\\ \mathbf{0}\,\mathbf{0}\,\mathbf{0}\,\mathbf{0}\\ \mathbf{0}\,\mathbf{0}\,\mathbf{0}\,\mathbf{0}\end{pmatrix},\quad \mathbf{R}=\begin{pmatrix}\mathbf{0}\,\mathbf{0}\,\mathbf{0}\,\mathbf{0}\\ \mathbf{0}\,\mathbf{0}\,\mathbf{I}\,\mathbf{0}\\ \mathbf{0}\,\mathbf{0}\,\mathbf{0}\,\mathbf{0}\\ \mathbf{0}\,\mathbf{0}\,\mathbf{0}\,\mathbf{0}\end{pmatrix}\tag{15}$$

in Eq. (12) are defined to fulfill the boundary conditions Eq. (6), while coefficient matrix

$$\mathbf{Q}=\begin{pmatrix}\mathbf{0} & \mathbf{0} & \mathbf{0} & \mathbf{0}\\ \mathbf{0} & \mathbf{0} & \mathbf{0} & \mathbf{0}\\ \mathbf{I} & \mathbf{0} & -\mathbf{I} & \mathbf{0}\\ \mathbf{0} & I_{\mathrm{z}1}E\mathbf{I} & \mathbf{0} & -I_{\mathrm{z}2}E\mathbf{I}\end{pmatrix}\tag{16}$$

comes from the interface condition Eq. (7). In Eqs. (15) and (16), where $\mathbf{I}$ and $\mathbf{0}$ stand for 2×2 identity and zero matrices, respectively.

The homogeneous solution of Eq. (11) is

$$\boldsymbol{\eta}(x,s)=\mathrm{e}^{\mathbf{A}(s)x}\boldsymbol{\eta}(0,s)\tag{17}$$

where $\mathrm{e}^{\mathbf{A}(s)x}$ is the exponential of matrix $\mathbf{A}(s)x$, also called fundamental matrix. Substitute Eq. (17) into the boundary conditions Eq. (12):

$$\left(\mathbf{P}+\mathbf{Q}\mathrm{e}^{\mathbf{A}(s)e}+\mathbf{R}\mathrm{e}^{\mathbf{A}(s)L}\right)\boldsymbol{\eta}(0,s)=\mathbf{0}.\tag{18}$$

The eigenvalues of the continuum model are the roots s_k of the transcendent characteristic equation

$$\det\left(\mathbf{P}+\mathbf{Q}\mathrm{e}^{\mathbf{A}(s)e}+\mathbf{R}\mathrm{e}^{\mathbf{A}(s)L}\right)=0, \tag{19}$$

which can be used to extract the modal parameters

$$s_k=-\zeta_k\omega_{\mathrm{n},k}\pm\mathrm{i}\omega_{\mathrm{n},k}\sqrt{1-\zeta_k^2},\quad k=1,\ldots,\tilde{m}. \tag{20}$$

Note that this result can be used to validate the parameters of the FEM, however, the challenging root finding problem of Eq. (19) is not necessary to determine the exact FRF.

According to [30], the unique solution of Eq. (11), which satisfies the boundary conditions Eq. (12), can be written in the following form

$$\boldsymbol{\eta}(x,s)=\int_0^L\mathbf{G}(x,\vartheta,s)\mathbf{q}(\vartheta,s)\mathrm{d}\vartheta, \tag{21}$$

where the matrix Green function is given as

$$\mathbf{G}(x,\vartheta,s)=\begin{cases}\mathbf{W}(x,s)\mathbf{P}\mathrm{e}^{-\mathbf{A}(s)\vartheta} & \text{if}\quad x\geq\vartheta,\\ -\mathbf{W}(x,s)\mathbf{R}\mathrm{e}^{\mathbf{A}(s)(L-\vartheta)} & \text{if}\quad x<\vartheta\end{cases} \tag{22}$$

and

$$\mathbf{W}(x,s)=\mathrm{e}^{\mathbf{A}(s)x}\left(\mathbf{P}+\mathbf{Q}\mathrm{e}^{\mathbf{A}(s)e}+\mathbf{R}\mathrm{e}^{\mathbf{A}(s)L}\right)^{-1}. \tag{23}$$

Finally, the exact scalar valued direct FRF $H(\omega,e)$ at the contact point of the tool can be calculated by means of the substitution of $x=\vartheta=e$ and $s=\mathrm{i}\omega$ into Eq. (22) and by selecting the matrix element 1,4

$$H(\omega,e)=\frac{G_{1,4}(e,e,\mathrm{i}\omega)}{I_{\mathrm{z}1}E(1+\mathrm{i}\omega\alpha_{\mathrm{K}})} \tag{24}$$

The indexes in $G_{1,4}(e,e,\mathrm{i}\omega)$ refer to the corresponding 1st element of the state space vector in Eq. (9) and the 4th element of the excitation vector Eq. (10).

It should be noted that the DTFM can give exact and closed-form solution of the FRF without any truncation or approximation by using only the inverse and the exponent of 8×8 matrices.

2.3 Validation of FE model

The convergence of natural frequencies and mode shapes regarding to element size of FE model is well-established. Since for the stability calculation of milling process a full FRF function is needed, and the effects of the FE model parameters on the FRF function is not so common, therefore, in this subsection, the convergence analysis of the FEM is based on the exact analytical solution of the continuum model. First, the resolution of the FE mesh is investigated through the comparison of the essential natural frequencies in order to determine sufficient element size. The relative error between the exact natural frequencies calculated with DTFM and the ones obtained from FEM is

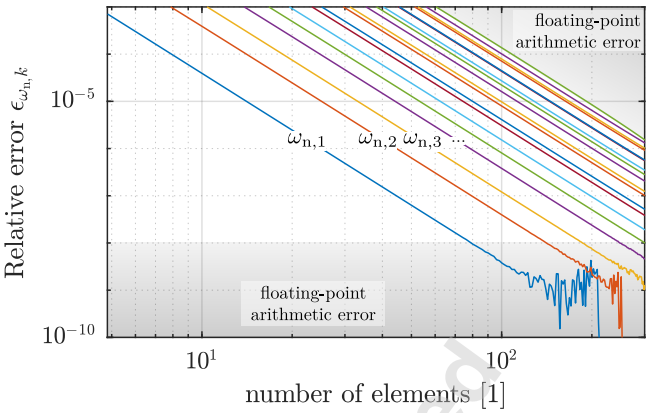

Fig. 2. Relative error of the natural frequencies as a function of the number of elements at $e=L/2$. Parameters are defined in Table 1 for Workpiece I.

$$\varepsilon_{\omega_{\mathrm{n},k}}=\frac{|\omega_{\mathrm{n},k}-\tilde{\omega}_{\mathrm{n},k}|}{\omega_{\mathrm{n},k}}. \tag{25}$$

Figure 2 shows the 4th-order convergence of each natural frequency which belongs to the Bernoulli beam-type finite elements. The convergence is limited by the floating-point arithmetic in two ways. On the one hand, numerical noise appears below the relative error around 10^{-8} for both DTFM and FEM. On the other hand, numerical errors accumulate in the iterative method applied for the solution of the eigenvalue problem, which is typical for higher frequencies. From Fig. 2, one can select an appropriate element resolution to keep the relative error within a desired range. For further investigation, we select 100 elements along the workpiece.

As a next step, the reduction of the number $\tilde{m}$ of the considered modes in Eq. (4) is investigated based on the deviation in the resulted FRF. The relative error between the exact direct FRF $H(\omega,e)$ and the one computed by FEM $\tilde{H}(\omega,e)$ is given by means of the formula

$$\varepsilon_H=\frac{\int_0^L\int_0^{\omega_{\max}}|H(\omega,e)-\tilde{H}(\omega,e)|\mathrm{d}\omega\mathrm{d}e}{\int_0^L\int_0^{\omega_{\max}}|H(\omega,e)|\mathrm{d}\omega\mathrm{d}e} \tag{26}$$

applied for the investigated frequency domain $[0,\,\omega_{\max}]$. Figure 3 represents the relative errors in a logarithmic scale for different domains, which cover a couple of essential natural frequencies. It is easy to show that the relative error decreases by increasing the number of considered modes. Note that even if we liked to model the first two natural frequencies only in the direct FRF with $\omega_{\max}=4500$ Hz, then at least twenty modes ($\tilde{m}\geq20$) should be considered to achieve a high accuracy like $\varepsilon_H=10^{-4}$.

Journal of Manufacturing Science and Engineering. Received June 04, 2019;
Accepted manuscript posted October 28, 2019. doi:10.1115/1.4045418

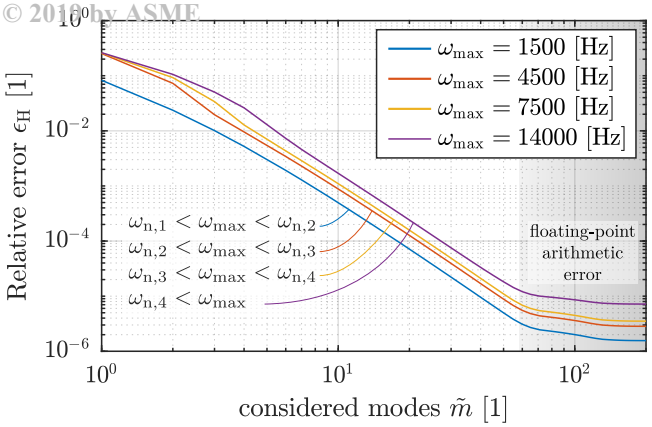

Fig. 3. The convergence of the relative error in the function of considered mode number for the different frequency domains $[0, \omega_{max}]$. Parameters are defined in Table 1 for Workpiece I.

Table 1. Parameters of the milled workpieces (Workpiece I. and II.)

Parameter	Symbol	Workp. I.	Workp. II.
Width	w	15 [mm]	20 [mm]
Thickness	v_2	3 [mm]	5 [mm]
Length	L	105 [mm]	
Material		AlMgSi05	
Density	ρ	2935 $[\frac{kg}{m^3}]$	
Young's modulus	E	50 [GPa]	
Stiffness prop. damping coeff.	α_K	$1.43 \cdot 10^{-6}$ [s]	
Mass prop. damping coeff.	α_M	45 $[\frac{1}{s}]$	

Also, the achievable accuracy in case of more than fifty modes is strongly limited by the errors generated by the floating-point arithmetic. If ω_{max} is selected for the bandwidth of the given excitation, then appropriate number of modes can be selected with the help of the diagram in Fig. 3.

As a conclusion, to capture the chatter frequency, usually the first or the second "lobe rows" play a role, which is closely related to the first and second natural frequencies. So one might choose only one or two natural frequencies, however, not only the first few modes are relevant to create the proper FRF. Therefore, high number of modes have to be considered in this type of modeling, consequently, it requires good resolution of the FE mesh, as well.

3 Analysis of varying dynamics

In this section we analyze the variation of the dynamic properties along the tool path during the material removal.

In Fig. 4, the amplitude of the direct FRF (colormap) and the natural frequencies (dashed curves) are presented for

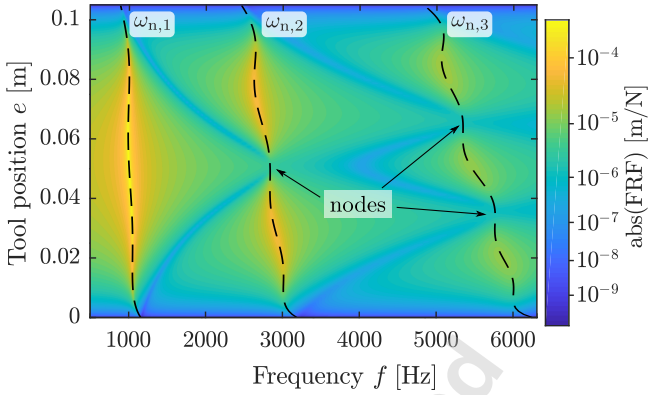

Fig. 4. Direct FRF of the workpiece at the actual tool position, where the thickness of the plate was reduced by 16.7%. The amplitude and the natural frequencies are denoted by colormap and dashed black curves, respectively. Parameters are presented for Workpiece I. in Table 1.

different tool positions. The natural frequencies of a prismatic beam are linearly proportional to the thickness of the cross-section, which is v for rectangular and d for cylindrical cross-section. Thus, the natural frequencies at the end position ($e = L$) of the tool are 16.7% smaller than they are at its starting position ($e = 0$); for example, $\omega_1(0) = 1155$ Hz $\rightarrow \omega_1(L) = 958$ Hz. However, during the material removal process, the natural frequencies change in an intricate way; it can increase or decrease whether the mass or the stiffness reduction has larger influence. In the colormap of Fig. 4, the variation of the abs(FRF) peaks is proportional to the corresponding mode shapes. It also visualizes that the workpiece is ideally stiff at both ends, moreover, it is dynamically stiff at the nodes of the corresponding mode shapes.

The effects of material removal can be visualized better in Fig. 5, where the relative frequency change for first and second natural frequencies are represented along the tool path for different amount of material removal. The larger the cross-section reduction is, the more the natural frequency values fluctuate. In an extreme reduction (close to 100%) as an illustrative example, it tends to a specific characteristic, referred to as backbone curve of the material removal.

This limitcase can be given if the system is decomposed into two separate beam segments while the connection between them is replaced by different boundary conditions (see the schematic representation in Fig. 6). If we consider a very high stiffness ratio of the parts, then the stiffer (thick blue) beam is not influenced by the more flexible (thin red) one and the stiffer beam can be modelled as a cantilever beam. Meanwhile, the upper end of the more flexible beam is almost fixed by the stiffer one, so it can be modelled as clamped-clamped beam. The corresponding natural frequencies can be determined from the following frequency equations [40], for the cantilever beam as

$$\cos\left((L-e)\sqrt[4]{\omega_n^2 \frac{A_2\rho}{I_{z2}E}}\right)\cosh\left((L-e)\sqrt[4]{\omega_n^2 \frac{A_2\rho}{I_{z2}E}}\right) = -1. \quad (27)$$

Journal of Manufacturing Science and Engineering. Received June 04, 2019;
Accepted manuscript posted October 28, 2019. doi:10.1115/1.4045418

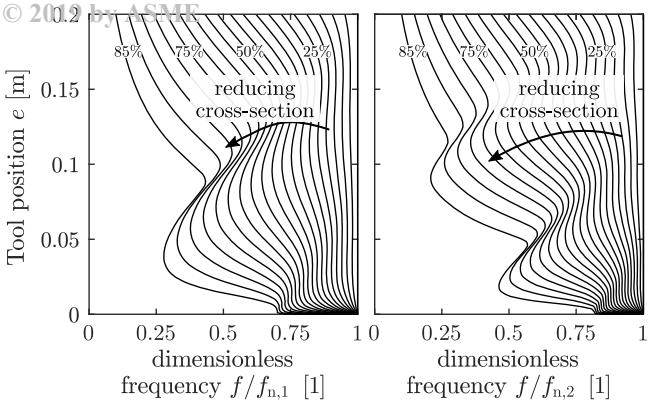

Fig. 5. Characteristics of the dimensionless natural frequencies as a function of the tool position for different cross-section removal rate.

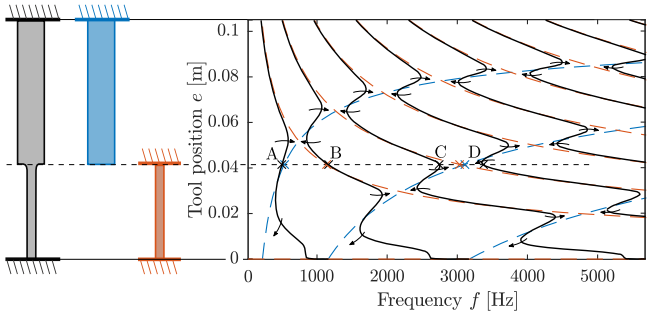

Fig. 6. Decomposition of the beam model; black curves represents natural frequencies in case of 85% cross section reduction, while blue and red dashed curves represent the natural frequencies of cross section reduction tending to 100%.

and for clamped-clamped beam as

$$\cos\left(e\sqrt[4]{\omega_{\mathrm{n}}^2\frac{A_1\rho}{I_{z1}E}}\right)\cosh\left(e\sqrt[4]{\omega_{\mathrm{n}}^2\frac{A_1\rho}{I_{z1}E}}\right)=1, \tag{28}$$

The natural frequencies of the decomposed models (solutions of Eq. (27) and (28)) are plotted by blue and red dashed curves, while natural frequencies relating to the original model are plotted by black curves for 85% cross-section reduction in Fig. 6.

Intersections of two backbones curves can be considered as attractive points, to which the curves of the natural frequencies tend (see points A and B in Fig. 6). Between these points, the natural frequencies of the original model follow one of the backbone curve. In the meantime, close to the attractive points, they swap to another backbone curve, where two adjacent frequencies are close to each other (see for example, points C and D in Fig. 6). With the proposed decomposition method, the pattern in the fluctuation of the natural frequencies can be identified and visualized.

Recall that the presented workpiece models can be used for milling and turning operations, as well. In the next section, the cutting force is derived for the milling process, and for the turning process, it can be obtained as its special case.

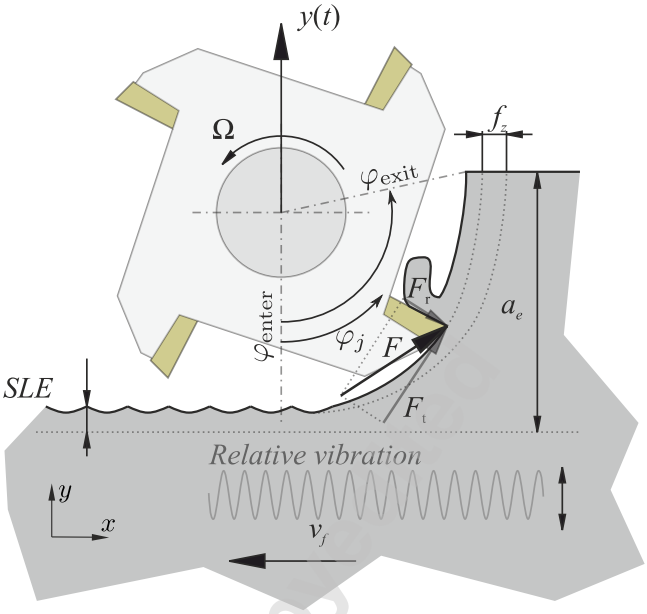

Fig. 7. Model of the milling process.

4 Milling process

To achieve the stability calculation and to anticipate the quality of the machined surface, the cutting operation of the milling process is described.

4.1 Cutting force

The widespread linear cutting force characteristic is applied, where the cutting force is linearly proportional to the instantenous chip thickness [41]. It can provide a good estimation for the forced vibration [42] and can suitably describe the chatter pehonena [4], as well. Note that description of models for general milling tool can be found in [43], but in our analysis, we focus on the description of traditional helical end-mills, only. The radial and the tangential components of the elementary cutting forces acting on an elementary segment $\mathrm{d}z$ of the j^{th} cutting edge (see Fig. 7) are given as

$$\begin{aligned}\mathrm{d}F_{\mathrm{r},j}(t)&=K_{\mathrm{r}}g\big(\varphi_j(t,z)\big)h_j\big(\varphi_j(t,z)\big)\mathrm{d}z\cos\eta,\\ \mathrm{d}F_{\mathrm{t},j}(t)&=K_{\mathrm{t}}g\big(\varphi_j(t,z)\big)h_j\big(\varphi_j(t,z)\big)\mathrm{d}z\cos\eta,\end{aligned} \tag{29}$$

where K_{r} and K_{t} are the radial and the tangential cutting coefficients, respectively. These parameters are usually identified by several cutting experiments for given cutting parameters and tool geometry [44]. The screen function is

$$g(\varphi)=\begin{cases}1 & \text{if } \varphi_{\mathrm{enter}}<\varphi<\varphi_{\mathrm{exit}},\\ 0 & \text{otherwise}\end{cases} \tag{30}$$

which tracks whether the j^{th} edge is in contact with the material or not in case of radial depth of cut a_{e} (see Fig. 7). The angular position of the j^{th} cutting edge for constant helix angle and equally distributed teeth is

$$\varphi_j(t,z)=\Omega t+\frac{2\pi(j-1)}{Z}-\frac{2\pi z}{Zl_{\mathrm{p}}}, \tag{31}$$

where Z is the number of the cutting edges, Ω stands for the spindle speed in [rad/s], l_p is the helix pitch and $\eta = \arctan D\pi/(Zl_\mathrm{p})$ denotes the helix angle. Also, $h\big(\varphi_j(t,z)\big)$ denotes the actual chip thickness, which is the sum of the stationary $h_\mathrm{stat}\big(\varphi_j(t,z)\big)$ and the dynamic $h_\mathrm{dyn}\big(\varphi_j(t,z)\big)$ chip thicknesses [4]. The stationary one can be given as the projection of the feed per tooth f_z into the tool tip velocity direction, which translates into

$$h_\mathrm{stat}\big(\varphi_j(t,z)\big) = f_z \sin\varphi_j(t,z) \tag{32}$$

in case of circular tooth path approximation [2]. It should be noted that the stationary chip thickness affects only the forced stationary vibration, and it has no influence on the stability of the cutting process in case of linear cutting force function [15]. The dynamic chip thickness relates to the surface regenerative effect of the cutting operation [9], which is relevant in the stability analysis of the machining process [4]. It reads as

$$h_\mathrm{dyn}\big(\varphi_j(t,z)\big) = \big(y(e,t) - y(e,t-\tau)\big)\cos\varphi_j(t,z), \tag{33}$$

where $y(e,t)$ denotes the general coordinate that describes the motion of the workpiece relative to the tool at the contact point e (see in Fig. 7). Note that the delayed position $y(e,t-\tau)$ represents the vibration copied onto the surface caused by the preceding cutting edge, where $\tau = 2\pi/(\Omega Z)$ denotes the tooth passing period.

In order to obtain the resultant cutting force, we project the force components from the local tangential-radial coordinate system into the global $x-y$ coordinate system. Also note that the *SLE* computation requires the forced vibration perpendicular to the surface. This beam model is flexible only in this direction, so the $\mathrm{d}F_y(t)$ component is presented in the next steps. This elementary force components are integrated along the z coordinate for the axial depth of cut a_p to obtain

$$F_y(t) = \sum_{j=1}^{N} \int_{a_\mathrm{p}} \big[K_\mathrm{t}\ K_\mathrm{r}\big]\, h\big(\varphi_j(t,z)\big) g\Big(\big(\varphi_j(t,z)\big)\Big) \big[-\sin\varphi_j(t,z)\ \cos\varphi_j(t,z)\big]^T \mathrm{d}z. \tag{34}$$

Note that for certain axial depth of cut values like $a_\mathrm{p} = l_\mathrm{p}, 2l_\mathrm{p}, 3l_\mathrm{p}, \ldots$, also called trivial appropriate axial immersions [45, 42], the stationary component of the cutting force is constant in time (see illustration in Fig. 8.

By means of the above described force model, both the surface quality prediction and the stability calculation can be carried out.

4.2 Surface Location Error

In what follows, the calculation steps of *SLE* induced by the forced vibration are presented [45]. The machined surface profile is a result by the relative motion of the workpiece and the cutting edges. The forced stationary vibration of the contact point can be determined by means of the direct FRF $H(\omega,e)$ (Eqs. (4) or (24)) according to

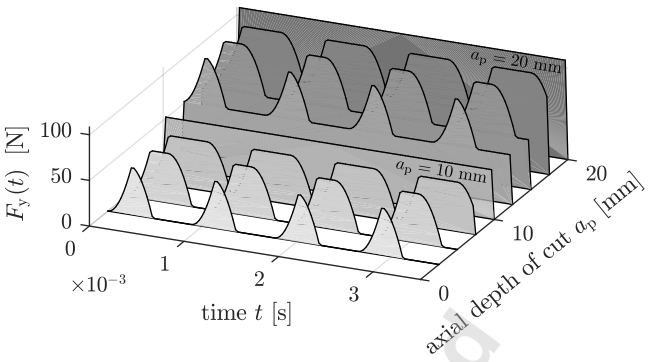

Fig. 8. Cutting force in different axial depth of cuts during one tool revolution for spindle speed $N = 17000$ rpm and helix pitch $l_\mathrm{p} = 10$ [mm]. Parameters are given in Tab. 2

$$y(e,t) = \mathscr{F}^{-1}\big(H(\omega,e)\phi_y(\omega)\big), \tag{35}$$

where $\phi_y(\omega)$ denotes the Fourier Transformation of the cutting force (34). The motion of the workpiece relative to the j^th cutting edge is described by means of the superposition of the rotating edges and the forced stationary vibration $y(e,t)$, that is

$$r_j(e,t,z) = y(e,t) - \frac{D}{2}\cos\varphi_j(t,z). \tag{36}$$

The *SLE* is determined as the extremum of these in the form

$$\begin{aligned} SLE(e,z) &= \max_{t,j}(r_j(e,t,z)) - \frac{D}{2} \quad \text{(up-milling)},\\ SLE(e,z) &= \min_{t,j}(r_j(e,t,z)) + \frac{D}{2} \quad \text{(down-milling)}. \end{aligned} \tag{37}$$

As a result, the $SLE(e,z)$ depends not on the tool position e only, but also on the axial coordinate z of the tool. Consequently, the so-called *Maximum Surface Location Error* $MSLE(e)$ parameter is introduced [45], which can be obtained by

$$MSLE(e) = \max_{z}(SLE(e,z)). \tag{38}$$

The described method is capable to forecast the *MSLE* values along the tool position for a given set of technological parameters. Note that this calculation is based on stable forced vibration, so it is valid only if the milling operation is in the chatter-free (stable) domain.

4.3 Stability analysis

In this section, the calculation of stability boundaries are briefly discussed according to the surface regenerative

Journal of Manufacturing Science and Engineering. Received June 04, 2019;
Accepted manuscript posted October 28, 2019. doi:10.1115/1.4045418

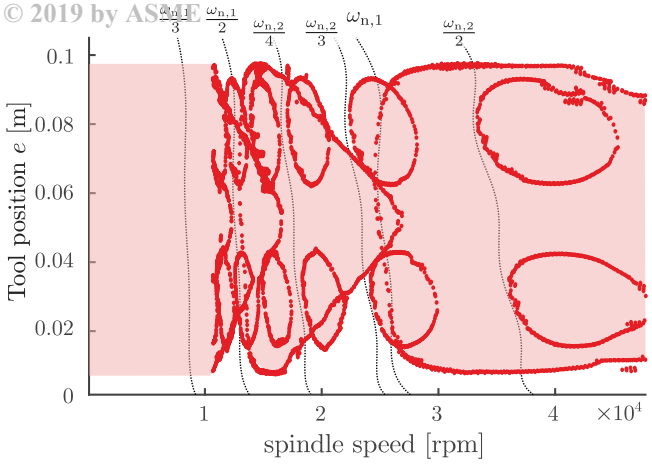

Fig. 9. Stability diagram in the plane of the tool path e and the spindle speed Ω. The red curves show the stability boundaries corresponding different vibration modes provided by the EMFS and the light red shaded area presents the corresponding unstable domains.

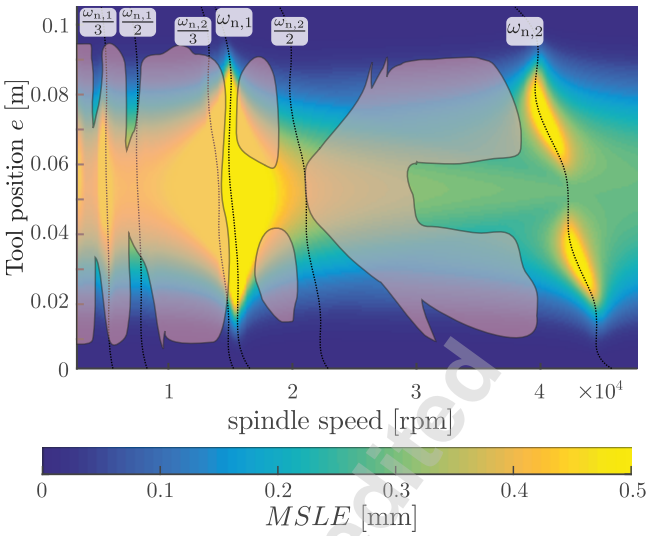

Fig. 10. The superchart with Maximum Surface Location Error and stability diagram in the plane of the spindle speed and the tool path for up-milling of Workpiece I; chatter appears within the pink domains. Parameters: $l_p = 10$ mm; $a_p = w = 15$ mm, $v = 3$ mm

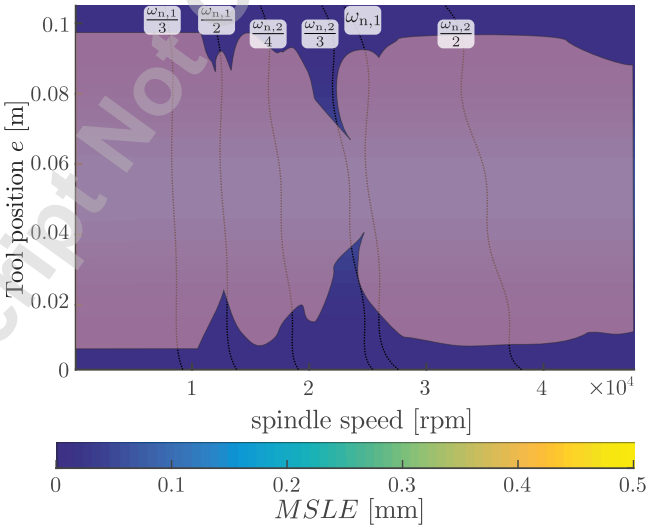

Fig. 11. The superchart with Maximum Surface Location Error and stability diagram in the plane of the spindle speed and the tool path for up-milling of Workpiece II; chatter appears within the pink domains. Parameters: $l_p = 10$ mm; $a_p = w = 20$ mm, $v = 5$ mm

effect, which is based on the method of the so-called Extended Multi Frequency Solution (EMFS) [11]. The EMFS is an effective computational algorithm in order to calculate the stability boundaries. It is based on the real and the imaginary parts of the truncated Hill's infinite determinant. Then, the stability chart is determined in the plane of the spindle speed Ω and the tool location e by means of the so-called Multi-Dimensional Bisection Method [46]. The combination of MDBM and EMFS is capable to determine the stability boundaries in a computationally effective way, even if closed stable or unstable islands appear. Figure 9 shows the stability chart for parameters presented in Table 1 and 2 considering that the entire width of the workpiece is machined ($a_p = w$). It should be noted that this stability diagram does not show the traditional lobe structure since the vertical axis is not the axial immersion a_p, but the tool position coordinate e. Still, the typical phenomenon, that one sides of the lobes tend to the natural frequencies or their integer quotients (ω_n/k, $k = 1, 2, ...$) can be observed in Fig. 9

5 Case study

In this section, the previously presented calculation methods are applied in two different case studies and compared to laboratory tests, for which, peripheral milling tests of beam-type workpieces are carried out with $w = a_p$. The technological parameters are shown in Table 1 and 2, the direct FRF is presented in Fig. 4.

5.1 Numerical results

The so-called superchart (see in Figs. 10 and 11) [16,45] visualizes the stability chart together with the *MSLE* values in the plane of the spindle speed N and the tool position coordinate e.

For the test case presented in Fig. 10, the chatter-free parameter regions (pockets) can be found among the stability lobes near to the resonant spindle speeds ($N \approx$ 15000, 21000, 41000 rpm). On the one hand, chatter can be avoided for the total length of the workpiece. On the other hand, these regions are usually not recommended from the viewpoint of the surface errors since significant resonant vibrations take place (see Fig. 10). However, it can be observed that negligible *MSLE* values are resulted along the spindle speed and tool position curves belonging to the angular frequencies $\omega_{n,1}/2$ and $\omega_{n,2}/2$.

Figure 11 shows the results of the second test with a wider workpiece where $w = a_p = 2l_p$. Accordingly, the cutting force does not vary in time and no resonance occurs that would generate large *MSLE*. In the meantime, however, the unstable region became larger due to the increased axial im-

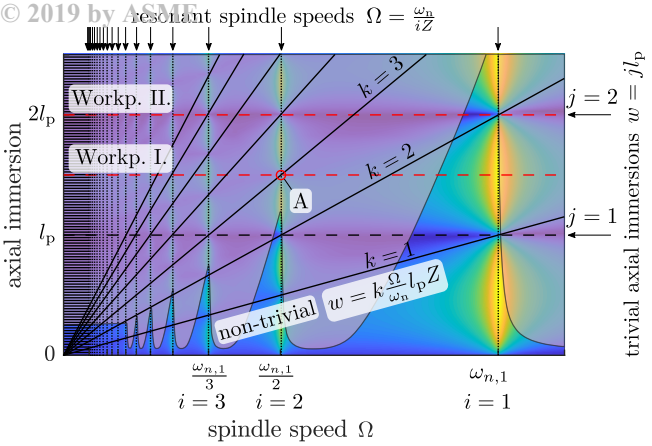

Fig. 12. Schematic representation of superchart with *MSLE* colormap and stability lobes in the plane of spindle speed and axial immersion together with the resonant spindle speeds (vertical dotted lines). The trivial appropriate axial immersions (horizontal dashed lines) and the non-trivial appropriate axial immersions (slanting black lines) are given for a single-degree-of-freedom milling model.

mersion.

It is well-known that large resonant stationary vibrations can occur if one of the natural frequencies is excited by one of the Fourier components of the cutting force variation. As a result, considerable *MSLE* can be generated at resonant spindle speeds

$$\Omega = \frac{\omega_n}{iZ}, i = 1,2,\dots, \tag{39}$$

which can be observed at the vertical dotted lines in Fig. 12. However, for helical cutting tools, there exist so-called trivial and non-trivial appropriate axial immersions [45, 42], where no resonant vibrations takes place and negligible *MSLE* can be realized even along these "resonant" vertical lines of the stability chart. The trivial appropriate axial immersion can be given by

$$w = jl_p, \quad j \in \mathbb{N}, \tag{40}$$

represented by horizontal dashed lines in Fig. 12. Note that in this case, the cutting edges cover full periods [0, $k2\pi$], thus, they result constant cutting force independently from the spindle speed Ω. The non-trivial appropriate axial immersion (see the slanting black lines in Fig. 12) can be given as

$$w(\Omega) = k\frac{\Omega}{\omega_n} l_p Z, \quad k \in \mathbb{N}, \tag{41}$$

for which, no resonant vibrations emerge at the "resonant" spindle speeds. This way, we can find low *MSLE* values for certain large axial immersions in the stable pockets along the vertical resonant spindle speed lines.

Table 2. Parameters of the case study [44]

Parameter	Symbol	Value
Feed per tooth	f_z	0.05 [mm]
Number of teeth	Z	4
Helix pitch	l_p	10 [mm]
Tool diameter	D	8 [mm]
Radial immersion	a_e	0.4 [mm]
Radial force coeff.	K_r	$300 \cdot 10^6 \left[\frac{N}{m^2}\right]$
Tang. force coeff.	K_r	$800 \cdot 10^6 \left[\frac{N}{m^2}\right]$

Fig. 13. Experimental setup

From practical point of view, the favorable cases are when the ratio of the helix pitch and width of the workpiece can be expressed as a ratio of two integers:

$$\frac{i}{k} = \frac{l_p}{w}, \quad i,k \in \mathbb{N} \tag{42}$$

in order to provide a condition for the number i of the higher harmonics of the resonant spindle speeds $\omega_n/(iZ)$ (see in Fig. 12).

In the case study of Workpiece I in Fig. 10, $l_p/w = 2/3$ and Eq. (42) holds for parameter pairs $[i,k]$ =[2,3], [4,6], [6,9], ... This means, that every second (even) resonant spindle speeds lead to negligible *MSLE* values (e.g.: $\omega_{n,1}/2$ relates to point A in Fig. 12), while the odd ones create resonant vibrations and large surface errors.

In the case study of Workpiece II in Fig. 11, $l_p/w = 1/2$ and Eq. (42) is hold for parameter pairs $[i,k]$ =[1,2], [2,4],[3,6], ... , which means that none of the "resonant" spindle speeds lead to resonance. This case demonstrate a special case, where the axial immersion a_p is the double of the helix pitch l_p, hence, this situation corresponds to the trivial appropriate axial immersion which relates to the horizontal red dashed line at $w = 2l_p$ in Fig. 12. Thus, the cutting force is constant, there is no forced vibration and the small *MSLE* is determined by the static deformation only.

Journal of Manufacturing Science and Engineering. Received June 04, 2019;
Accepted manuscript posted October 28, 2019. doi:10.1115/1.4045418

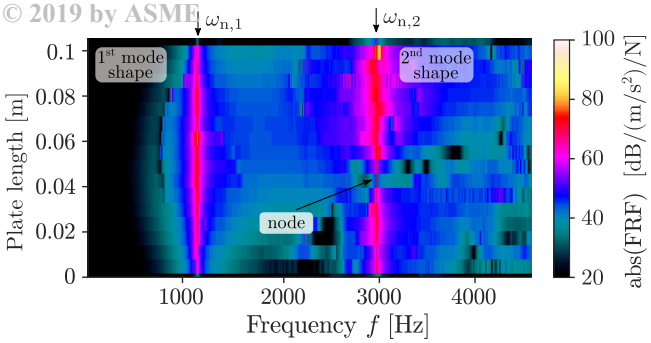

Fig. 14. FRF of Workpiece I along the tool position (waterfall diagram) for the first two natural frequencies and mode shapes.

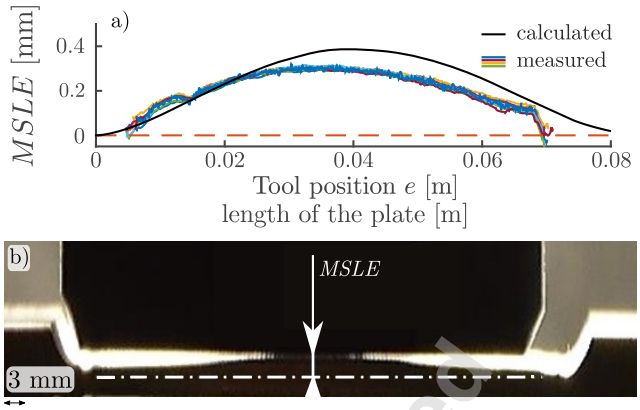

Fig. 15. Measured surface profile at along the workpiece (a) and scaled photo of the surface contour (b) in the function of the tool position for spindle speed $N = 17000$ rpm; parameters from Table 1 and 2 for Workpiece I.

Table 3. Natural frequencies of Workpiece I. before machining (see Fig. 14 and Fig. 4 at $e = 0$ [m])

	$\omega_{n,1}$	$\omega_{n,2}$
calculated	1142 [Hz]	3155 [Hz]
measured	1099 [Hz]	2914 [Hz]
relative err.	3,77 %	7.64 %

5.2 Measurement results

Measurements were performed both on Workpiece I and II fixed as a clamped-clamped beam in the NCT EmR-610Ms 3 axis CNC milling machine. The photo of the experimental setup is presented in Fig. 13. The corresponding parameters are presented in Table 1 and 2, which were identified by modal analysis and cutting tests [44, 41].

The FRF along the tool path for Workpiece I before the milling operation was measured by modal testing where the workpiece was excited at different positions. The first two natural frequencies and the corresponding mode shapes are visualized in a Pulse B&K data acquisition system, as shown in Fig. 14. Note that in this case, the natural frequencies do not change along the plate length, since there is no changing geometry. The predicted natural frequencies of the equivalent model can be seen from Fig. 4 at $e = 0$ m, and they are compared to the measured values in Table 3. It should be noted that there was a slight difference between the measured and the predicted natural frequencies (3,77 % and 7.64%). The major effect of the discrepancies can be the ideal modeling of the clamped-clamped ends, which may be too strict condition in practice. For accurate modeling of the clampings, it could be replaced by flexibel spring-damper elements, which parameters can be tuned. There is a mild asymmetry in the mode shapes, which also indicates not symmetrical clamping conditions. For our investigation, this difference ($< 8\%$) is acceptable, because, only to the change of the workpiece dynamics is in the focus of the paper. Thus, the effects and description of the optimized constraints are out of scope of this paper, although there exist several models in the literature [31, 27].

The first measurement was performed for Workpiece I at $N = 17000$ rpm, which is close to the first resonant spindle speed belonging to the first natural frequency of the workpiece. Fig. 15 shows the scaled photo of the surface contour of the workpiece and its laser scanned profile (colored curves) together with the theoretically predicted values (black curve). The detailed surface profile measurement method is presented in [47]. It can be seen, that the pattern of the large *MSLE* along the length of the workpiece has similar form to the respective first mode shape. In this test, no chatter marks were observed. Similar shape were predicted in Fig. 10 based on the numerical analysis of the corresponding mechanical model, but the asymmetry resulted from the different clampings was not captured by the model. As Fig. 15 shows, there is a slight difference between the measured and predicted surface profile (black curve). Since the amplitude of the resulting vibration, consequently, the magnitude of surface errors are depending on the "distance" from the resonant spindle speed, a slight deviation in the natural frequencies may cause this discrepancy in the magnitude of the surface errors.

The spindle speed $N = 22000$ rpm was also tested which is near to the second resonant spindle speed belonging to the second natural frequency. In this case, only negligible *MSLE* values were measured as predicted in Eq. (42) for $[i,k]$ $=[2,3]$. However, chatter marks can be observed in regions according to the second mode shape shown in Fig. 16; this is also presented by the high fluctuations of the measured surface profile. The reasons for this could be that the domain of the two unstable islands are underestimated and the line of the selected spindle speed crosses them in the chart Fig. 10.

During the measurement performed for Workpiece II, we find chatter marks along the whole workpiece for all the tested spindle speeds as predicted by the numerical results in Fig. 11. The spectrogram of a typical vibration signal is shown in Fig. 17, which represents that the varying chatter frequency along the tool path relates to the fluctuated natural frequency. Note that, there is no one single dominant chat-

Journal of Manufacturing Science and Engineering. Received June 04, 2019;
Accepted manuscript posted October 28, 2019. doi:10.1115/1.4045418

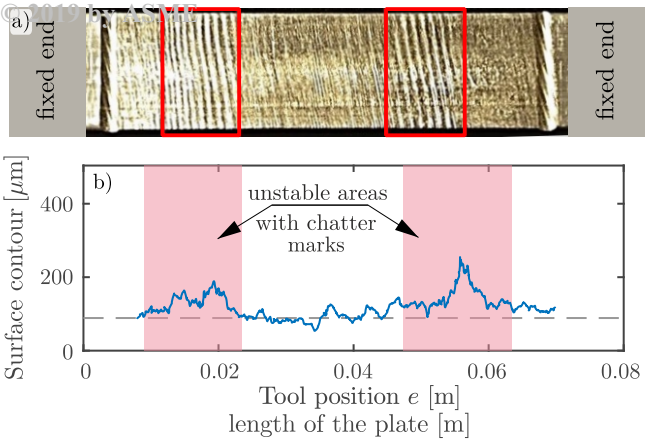

Fig. 16. Photo of the chatter marks (a) and the laser scanned surface profile (b) for Workpiece I at spindle speed $N = 22000$ rpm; parameters from Table 1 and 2.

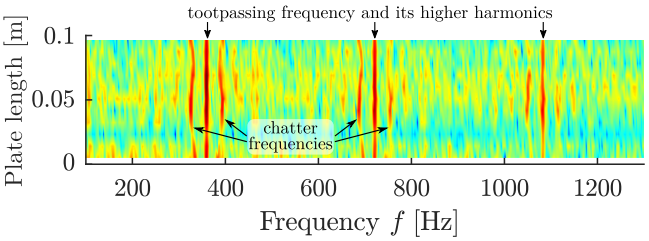

Fig. 17. Typical spectrum for a fully unstable milling case at spindle speed $N = 21660$ rpm.

ter frequencies, but multiple ones, which is typical in highly interrupted milling [48]. As an example, the machined surface at $N = 17000$ rpm is presented in Fig. 18, which shows chatter marks along the full length of the tool path. Note that negligible shape deviation is detected, because trivial appropriate axial immersion is applied (see Eq. (40) for $a_p = 2l_p$).

All the results of the performed measurements are in correlation with the theoretical predictions. The measurements also show that the varying dynamical properties has relevant influence on the surface errors and the stability properties in case of flexible workpieces. The differences can be explained by the non-ideal and non-symmetric clampings, which may lead to change in natural frequencies, asymmetry in mode shapes and consequently, in surface errors.

All the above presented steps of MSLE and stability computation can be performed in case of more complex geometry. However, in a general situation, analytical solution may not exist, but from a detailed FE model one can compute the FRF along the tool path. With this extended FRF, the stability chart and the surface quality can be predicted at each step along the tool path. Based on these methodology, the cutting technology of the milling operations can be optimized in order to achieve efficient production and reach acceptable surface errors.

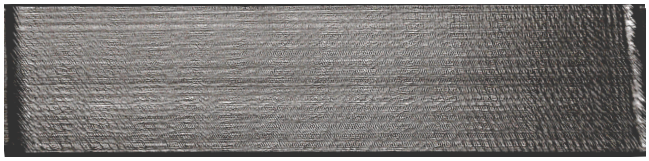

Fig. 18. Chatter marks on the milled surface for Workpiece II at $N = 17000$ rpm; parameters from Table 1 and 2.

6 Conclusions

In this contribution, it is shown how the change of the Frequency Response Function affect the stability and surface errors of the milling operations. To demonstrate this, the workpiece is considered as a flexible beam, moreover, the stiffness variation caused by the material removal and the change in the excitation point (tool position) are also taken into consideration. First, finite element formulation is derived for the direct Frequency Response Function, then its parameters are validated through an analytical closed form solution (called distributed transfer function method). The pattern of the natural frequency fluctuation caused by the material removal is explained through extreme cross-section reduction, for which, analytical solution is provided in the limit case.

The stability boundaries together with the *MSLE* values are presented in the superchart as a function of spindle speed and tool position.

The case studies show that the chatter-free parameter domains are located at the resonant spindle speeds. It is also shown that the Maximum Surface Location Errors can be significant at these spindle speeds. However, if the trivial or the non-trivial appropriate axial immersions are applied, then good surface quality can be achieved even for resonant spindle speeds. In this sense, the results of this paper may help understanding the connections between the mode shapes/natural frequencies and the location of the unstable areas and surface errors. The numerical and the experimental case studies show agreement, which validates the theoretical predictions.

Acknowledgements

The research reported in this paper has been supported by the National Research, Development and Innovation Fund (TUDFO/51757/2019-ITM, Thematic Excellence Program). The research reported in this paper was supported by the Higher Education Excellence Program of the Ministry of Human Capacities in the frame of Artificial intelligence research area of Budapest University of Technology and Economics (BME FIKP-MI). This paper was supported by the Hungarian Scientific Research Fund OTKA FK-124462 and PD-124646.

References

[1] Tlusty, J., and Spacek, L., 1954. *Self-excited vibrations on machine tools*. Nakl. CSAV, Prague. in Czech.

[2] Tobias, S., 1965. *Machine-tool Vibration*. Blackie, Glasgow.

[3] Stepan, G., 1989. *Retarded dynamical systems*. Longman, Harlow.

[4] Insperger, T., and Stepan, G., 2011. *Semi-discretization for time-delay systems*, Vol. 178. Springer, New York.

[5] Ding, Y., Zhu, L. M., Zhang, X. J., and Ding, H., 2010. "A full-discretization method for prediction of milling stability". *Int J Mach Tool Manu,* **50**, pp. 502–509.

[6] Zhang, X. J., Xiong, C. H., Ding, Y., Feng, M. J., and Xiong, Y. L., 2012. "Milling stability analysis with simultaneously considering the structural mode coupling effect and regenarative effect". *Int J Mach Tool Manu,* **53**, pp. 127–140.

[7] Totis, G., Albertelli, P., Sortino, M., and Monno, M., 2014. "Efficient evaluation of process stability in milling with spindle speed variation by using the chebyshev collocation method". *J Sound Vib,* **333**, pp. 646–668.

[8] Bayly, P. V., Halley, J. E., Mann, B. P., and Davies, M. A., 2003. "Stability of interrupted cutting by temporal finite element analysis". *Journal of Manufacturing Science and Engineering,* **125**, pp. 220–225.

[9] Altintas, Y., and Budak, E., 1995. "Analytical prediction of stability lobes in milling". *CIRP Ann-Manuf Techn,* **44**, pp. 357–362.

[10] Budak, E., and Altintas, Y., 1998. "Analytical prediction of chatter stability in milling, part i: General formulation". *J Dyn System ASME,* **120**, pp. 22–30.

[11] Bachrathy, D., and Stepan, G., 2013. "Improved prediction of stability lobes with extended multi frequency solution". *CIRP Ann-Manuf Techn,* **62**, pp. 411–414.

[12] Davim, J., 2001. "A note on the determination of optimal cutting conditions for surface finish obtained in turning using design of experiments". *Journal of Materials Processing Technology,* **116**(2), pp. 305 – 308.

[13] Budak, E., and Altintas, Y., 1995. "Modeling and avoidance of static form errors in peripheral milling of plates". *International Journal of Machine Tools and Manufacture,* **35**(3), pp. 459 – 476.

[14] Schmitz, T. L., and Mann, B. P., 2006. "Closed-form solutions for surface location error in milling". *International Journal of Machine Tools and Manufacture,* **46**(12), pp. 1369 – 1377.

[15] Insperger, T., Gradisek, J., Kalveram, M., Stepan, G., Winert, K., and Govekar, E., 2006. "Machine tool chatter and surface location error in milling processes". *Journal of Manufacturing Science and Engineering,* **128**, pp. 913–920.

[16] Zapata, R., DeMarco, C., and Schmitz, T., 2008. "The milling dynamics "super diagram": Combining stability and surface location error". In Proceedings of American Society for Precision Engineering Annual Meeting.

[17] Budak, E., Tunc, L., Alan, S., and Özgüven, H. N., 2012. "Prediction of workpiece dynamics and its effects on chatter stability in milling". *CIRP Annals,* **61**(1), pp. 339 – 342.

[18] Bravo, U., Altuzarra, O., de Lacalle, L. L., Sánchez, J., and Campa, F., 2005. "Stability limits of milling considering the flexibility of the workpiece and the machine". *International Journal of Machine Tools and Manufacture,* **45**(15), pp. 1669 – 1680.

[19] Thevenot, V., Arnaud, L., Dessein, G., and Cazenave–Larroche, G., 2006. "Influence of material removal on the dynamic behavior of thin-walled structures in peripheral milling". *Machining Science and Technology,* **10**(3), pp. 275–287.

[20] Denkena, B., and Schmidt, C., 2007. "Experimental investigation and simulation of machining thin-walled workpieces". *Production Engineering,* **1**(4), pp. 343–350.

[21] Otto, A., Khasawneh, F. A., and Radons, G., 2015. "Position-dependent stability analysis of turning with tool and workpiece compliance". *The International Journal of Advanced Manufacturing Technology,* **79**(9), pp. 1453 – 1463.

[22] Seguy, S., Dessein, G., and Arnaud, L., 2008. "Surface roughness variation of thin wall milling, related to modal interactions". *International Journal of Machine Tools and Manufacture,* **48**(3), pp. 261 – 274.

[23] Li, Z.-L., Tuysuz, O., Zhu, L.-M., and Altintas, Y., 2018. "Surface form error prediction in five-axis flank milling of thin-walled parts". *International Journal of Machine Tools and Manufacture,* **128**, pp. 21 – 32.

[24] Song, Q., Ai, X., and Tang, W., 2011. "Prediction of simultaneous dynamic stability limit of time–variable parameters system in thin-walled workpiece high-speed milling processes". *The International Journal of Advanced Manufacturing Technology,* **55**(9), pp. 883–889.

[25] Tuysuz, O., and Altintas, Y., 2017. "Frequency domain updating of thin-walled workpiece dynamics using reduced order substructuring method in machining". *Journal of Manufacturing Science and Engineering,* **139**(7), p. 071013.

[26] Yang, Y., Zhang, W.-H., Ma, Y.-C., Wan, M., and Dang, X.-B., 2019. "An efficient decomposition-condensation method for chatter prediction in milling large-scale thin-walled structures". *Mechanical Systems and Signal Processing,* **121**, pp. 58 – 76.

[27] Stepan, G., Kiss, A. K., Ghalamchi, B., Sopanen, J., and Bachrathy, D., 2017. "Chatter avoidance in cutting highly flexible workpieces". *CIRP Annals,* **66**(1), pp. 377–380.

[28] Kiss, A. K., Bachrathy, D., and Stepan, G., 2016. "Surface error and stability chart of beam-type workpiece in milling processes". International Design Engineering Technical Conferences and Computers and Information in Engineering Conference, Volume 8: 28th Conference on Mechanical Vibration and Noise.

[29] Ewins, D. J., 2000. *Modal Testing, Theory, Practice, and Application*. Research Studies Press 2nd edition.

[30] Yang, B., and Tan, C. A., 1992. "Transfer functions of one-dimensional distributed parameter systems". *Journal of Applied Mechanics,* **59**(4), pp. 1009–1014.

[31] Mancisidor, I., Urkiola, A., Barcena, R., Munoa, J.,

Dombovari, Z., and Zatarain, M., 2014. "Receptance coupling for tool point dynamic prediction by fixed boundaries approach". *International Journal of Machine Tools and Manufacture,* **78**, pp. 18 – 29.

[32] Campa, F., de Lacalle, L. L., and Celaya, A., 2011. "Chatter avoidance in the milling of thin floors with bull-nose end mills: Model and stability diagrams". *International Journal of Machine Tools and Manufacture,* **51**(1), pp. 43 – 53.

[33] Sellmeier, V., and Denkena, B., 2011. "Stable islands in the stability chart of milling processes due to unequal tooth pitch". *International Journal of Machine Tools and Manufacture,* **51**(2), pp. 152 – 164.

[34] Erneux, P., and Mandel, T., 1986. "Imperfect bifurcation with a slowly-varying control parameter". *SIAM Appl. Math,* **46**(1), pp. 1 – 16.

[35] Haberman, R., 1979. "Slowly-varying jump and transition phenomena associated with algebraic bifurcation problems". *SIAM J. Appl. Math,* **37**(1), pp. 69 – 106.

[36] Dombovari, Z., Munoa, J., Kuske, R., and Stepan, G., 2018. "Milling stability for slowly varying parameters". *Procedia CIRP,* **77**, pp. 110 – 113. 8th CIRP Conference on High Performance Cutting (HPC 2018).

[37] Timoshenko, S., and Goodier, J., 1969. *Theory of elasticity*. McGraw-Hill classic textbook reissue series. McGraw-Hill.

[38] Butkovskiy, A. G., 1983. *Structural Theory of Distributed Systems*. Prentice Hall Europe.

[39] Schmitz, T., and Donalson, R., 2000. "Predicting high-speed machining dynamics by substructure analysis". *CIRP Annals,* **49**(1), pp. 303 – 308.

[40] Rao, S. S., 2007. *Vibration of Continuous Systems*. John Wiley & Sons, Inc.

[41] Altintas, Y., 2012. *Manufacturing Automation - Metal Cutting Mechanics, Machine Tool Vibrations and CNC Design, Second Edition*. Cambridge University Press, Cambridge.

[42] Bachrathy, D., Munoa, J., and Stepan, G., 2015. "Experimental validation of appropriate axial immersions for helical mills". *The International Journal of Advanced Manufacturing Technology*, pp. 1–8.

[43] Dombovari, Z., and Stepan, G., 2012. "The effect of helix angle variation on milling stability". *Journal of Manufacturing Science and Engineering,* **134**(5), p. 051015.

[44] Budak, E., Altintas, Y., and Armarego, E. J. A., 1996. "Prediction of milling force coefficients from orthogonal cutting data". *Journal of Manufacturing Science and Engineering,* **118**(2), pp. 216–224.

[45] Bachrathy, D., Insperger, T., and Stepan, G., 2009. "Surface properties of the machined workpiece for helical mills". *Machining Science and Technology,* **13**(2), pp. 227–245.

[46] Bachrathy, D., and Stepan, G., 2012. "Bisection method in higher dimensions and the efficiency number". *Periodica Polytechnica Mechanical Engineering,* **56**(2), pp. 81–86.

[47] Kiss, A. K., Bachrathy, D., and Stepan, G., 2018. "Laser scanned patterns of machined surfaces". In 8th CIRP Conference on High Performance Cutting (HPC 2018), Vol. 77, Elsevier, Procedia CIRP 4, p. 355–358.

[48] Dombovari, Z., Iglesias, A., Zatarain, M., and Insperger, T., 2011. "Prediction of multiple dominant chatter frequencies in milling processes". *Int J Mach Tool Manu,* **51**, pp. 457–464.

list of table captions:

Table 1. Parameters of the milled workpieces (Workpiece I. and II.)

Table 2. Parameters of the case study [44]

Table 3. Natural frequencies of Workpiece I. before machining (see Fig. 14 and Fig. 4 at $e = 0$ [m])

list of figure captions:

Fig. 1. Schematic figure of the applied beam-type workpiece considering the material removal for milling (a) and turning (b) processes.

Fig. 2. Relative error of the natural frequencies as a function of the number of elements at $e = L/2$. Parameters are defined in Table 1 for Workpiece I.

Fig. 3. The convergence of the relative error in the function of considered mode number for the different frequency domains $[0, \omega_{\max}]$. Parameters are defined in Table 1 for Workpiece I.

Fig. 4. Direct FRF of the workpiece at the actual tool position, where the thickness of the plate was reduced by 16.7%. The amplitude and the natural frequencies are denoted by colormap and dashed black curves, respectively. Parameters are presented for Workpiece I. in Table 1.

Fig. 5. Characteristics of the dimensionless natural frequencies as a function of the tool position for different cross-section removal rate.

Fig. 6. Decomposition of the beam model; black curves represents natural frequencies in case of 85% cross section reduction, while blue and red dashed curves represent the natural frequencies of cross section reduction tending to 100%.

Fig. 7. Model of the milling process.

Fig. 8. Cutting force in different axial depth of cuts during one tool revolution for spindle speed $N = 17000$ rpm and helix pitch $l_p = 10$ [mm]. Parameters are given in Tab. 2

Fig. 9. Stability diagram in the plane of the tool path e and the spindle speed Ω. The red curves show the stability boundaries corresponding different vibration modes provided by the EMFS and the light red shaded area presents the corresponding unstable domains.

Fig. 10. The superchart with Maximum Surface Location Error and stability diagram in the plane of the spindle speed and the tool path for up-milling of Workpiece I; chatter appears within the pink domains. Parameters: $l_p = 10$ mm; $a_p = w = 15$ mm, $v = 3$ mm

Fig. 11. The superchart with Maximum Surface Location Error and stability diagram in the plane of the spindle speed and the tool path for up-milling of Workpiece II; chatter appears within the pink domains. Parameters: $l_p = 10$ mm; $a_p = w = 20$ mm, $v = 5$ mm

Fig. 12. Schematic representation of superchart with *MSLE* colormap and stability lobes in the plane of spindle speed and axial immersion together with the resonant spindle speeds (vertical dotted lines). The trivial appropriate axial immersions (horizontal dashed lines) and the non-trivial appropriate axial immersions (slanting black lines) are given for a single-degree-of-freedom milling model.

Fig. 13. Experimental setup

Fig. 14. FRF of Workpiece I along the tool position (waterfall diagram) for the first two natural frequencies and mode shapes.

Fig. 15. Measured surface profile at along the workpiece (a) and scaled photo of the surface contour (b) in the function of the tool position for spindle speed $N = 17000$ rpm; parameters from Table 1 and 2 for Workpiece I.

Fig. 16. Photo of the chatter marks (a) and the laser scanned surface profile (b) for Workpiece I at spindle speed $N = 22000$ rpm; parameters from Table 1 and 2.

Fig. 17. Typical spectrum for a fully unstable milling case at spindle speed $N = 21660$ rpm.

Fig. 18. Chatter marks on the milled surface for Workpiece II at $N = 17000$ rpm; parameters from Table 1 and 2.